Effect of anchoring dynamics on proton-coupled electron transfer in the Ru(bda) coordination oligomer on a graphitic surface

Calvani, D.; Louwersheimer, R.; Buda, F.

ChemPlusChem

Research Article
doi.org/10.1002/cplu.202400082

Chemistry Europe
European Chemical Societies Publishing

www.chempluschem.org

Effect of Anchoring Dynamics on Proton-Coupled Electron Transfer in the Ru(bda) Coordination Oligomer on a Graphitic Surface

Dario Calvani,*[a] Rick Louwersheimer,[a] and Francesco Buda*[a]

The oligomeric ruthenium-based water oxidation catalyst, Ru-(bda), is known to be experimentally anchored on graphitic surfaces through CH-π stacking interactions between the auxiliary bda ([2,2′-bipyridine]-6,6′-dicarboxylate) ligand bonded to ruthenium and the hexagonal rings of the surface. This anchoring provides control over their molecular coverage and enables efficient catalysis of water oxidation to dioxygen. The oligomeric nature of the molecule offers multiple anchoring sites at the surface, greatly enhancing the overall stability of the hybrid catalyst-graphitic surface anode through dynamic bonding. However, the impact of this dynamic anchoring on the overall catalytic mechanism is still a topic of debate. In this study, a crucial proton-coupled electron transfer event in the catalytic cycle is investigated using DFT-based molecular dynamics simulations plus metadynamics. The CH-π stacking anchoring plays a critical role not only in stabilizing this hybrid system but also in facilitating the proton-coupled electron transfer event with possible vibronic couplings between the anchoring bonds motion and charge fluctuations at the catalyst – graphitic surface interface. Furthermore, this computational investigation displays the presence of a quartet spin state intermediate that can lead to the experimentally observed and thermodynamically more stable doublet spin state.

Introduction

Over the past few decades, significant advancements have been made in the development of molecular water oxidation catalysts, reaching turnover frequencies (TOF) in the range of 50000 s^{-1}.[1–4] The success of molecular transition metal complexes as water oxidation catalysts is primarily due to their synthetic versatility and ability to allow for supramolecular interactions, hydrogen-bonding effects, and local acid-base enhancements.[5] Interestingly, the exploration of solid-surface-anchored molecular complexes as electro-anodes and cathodes for water-splitting devices has received relatively little attention, in particular when compared to non-molecular materials such as transition metal clusters[6] or nano-wires.[7] There are a few examples in the literature where molecular water oxidation catalysts have been modified with anchoring functionalities and successfully anchored onto conductive or semiconductive solid surfaces. These heterogenized, molecular hybrid materials exhibit varying degrees of performance and stability.[8–17] Concerning the anode, a crucial challenge lies in finding robust and efficient water oxidation catalysts (WOCs) that can be anchored onto a conductive or semiconductive surface.[18] Molecular catalysts offer a broad pH range for operation,[1–4,19–21] but their performance is often hindered by the limited amount of active catalyst that can be deposited per unit surface area.[22] Currently, in the range of the most promising molecular WOCs based on ruthenium complexes,[5,23,24] a family of Ru-tda-based oligomers of general formula $(Ru\text{-}tda)_n$ was prepared, isolated, and extensively characterized in a homogeneous solution by Hoque et al..[25] These oligomers demonstrate a remarkable affinity for graphitic surfaces like multiwalled carbon nanotubes (CNTs), owing to multiple ligand-based CH-π interactions with the graphitic surfaces,[25–28] and exhibiting impressive electrocatalytic activity for water oxidation as anchored molecular catalysts.[25] More recently, Gil-Sepulcre et al. explored the potential of Ru(bda) based catalysts as hybrid molecular WOCs. While monomeric Ru(bda) complexes have previously been shown to decompose when anchored to a surface,[29] Gil-Sepulcre et al. successfully anchored a decameric $Ru(bda)_{10}$ oligomer to the graphitic surface of CNTs and displayed excellent performance as water oxidation and outstanding stability.[30,31] They proposed a perpendicular CH-π interaction[25] between the CH groups of the bda ligands in the oligomer and the delocalized π-system of the graphitic material[30] to be responsible for the initial strong affinity of the oligomer towards the graphitic surface. Once anchored to the surface, the oligomeric catalyst can undergo a change of the bda ligand coordination mode at the electrode surface, transitioning from a bda-κ-N^2O^2 to a bda-κ-NO configuration, accompanied by the coordination of aqua ligands to the partially vacant positions left by the bda ligand.[30] They proposed that the bda-κ-NO coordinated $Ru(bda)_{10}$ oligomer interacts at the graphitic sur-

[a] D. Calvani, R. Louwersheimer, Dr. F. Buda
Leiden Institute of Chemistry
Leiden University
PO Box 9502, 2300 RA Leiden (The Netherlands)
E-mail: d.calvani@lic.leidenuniv.nl
f.buda@lic.leidenuniv.nl

Supporting information for this article is available on the WWW under https://doi.org/10.1002/cplu.202400082

face not only through CH-π interactions but also by introducing additional π-π and anion-π interactions involving the axial pyridyl moiety and the carboxylate group of the bda ligand, respectively.[30] Gil-Sepulcre et al. suggested that the anchoring interaction with the graphitic surface unlocks this transformation,[30] and proposed a separate more favorable catalytic cycle for the bda-κ-NO configuration with respect to the bda-κ-N^2O^2 case.[30] The dynamic CH-π interaction, indicated by Gil-Sepulcre et al., achieves surface densities that are significantly higher than traditional anchoring strategies based on π-π stacking, diazonium salts, or conventional methods,[32–34] resulting in exceptional stability.[30,31]

Therefore, a detailed analysis of the dynamics appears necessary to reveal the mechanistic features underlying the enhanced catalytic performance and stability of the Ru(bda)-based oligomer ($Ru(bda)_n$) anchored at the graphitic surface (GS). In this work, we computationally investigate the dynamics of the IV/V oxidation PCET step, as schematically shown in Figure 1, which appears to be strongly influenced by the catalyst anchoring conditions at the GS.[30] The main focus is to understand how the dynamics at the interface between the catalyst and the graphitic surface can affect the PCET event. A combination of DFT-based MD and metadynamics simulations have been efficiently used to explore the whole path of this specific PCET step from reactants to products and the spin states of the catalytic intermediates.[35,36] The stability of possible catalytic products with different spin states with respect to the reactant has been investigated and compared with the one experimentally predicted by Electron Paramagnetic Resonance (EPR).[30] Via a Vibrational Density Of States (VDOS) analysis, vibrational resonances between the dynamics at the anchoring region and the PCET event were studied. This analysis reveals strong resonances between specific nuclear frequencies and fluctuations in the Mulliken charges on the $Ru(bda)_n$ and GS. This computational work unveils the effect of the $Ru(bda)_n$ oligomer anchoring dynamics on the PCET event, stability of the anchored oligomer, and possible spin state intermediates at the base of the catalytic mechanism process.

Results and Discussion

Preliminary DFT-Based Static and MD Calculations

Initially, a static DFT geometry optimization of the $^3[^{\uparrow\uparrow}(Ru^{IV}\text{–}OH)(bda)_1]^0$ monomer catalyst in the triplet spin state, as predicted by Gil-Sepulcre et al.,[30] was performed to optimize the starting configuration of the PCET step (see Methods section). The unpaired electrons are indicated explicitly in the formulas near the corresponding molecular fragment, Ru(bda) complex or GS, as a ↑ or ↓ depending on the electron spin up (α) or down (β). Subsequently, the $^3[^{\uparrow\uparrow}(Ru^{IV}\text{–}OH)(bda)_1]^0$ optimized geometry was located above a GS at the optimal distance for an efficient CH-π stacking interaction.[26–28,30] The simulation box size of 11.30×12.78×16.00 $Å^3$ is chosen in such a way that the two picoline ligands without their para hydrogens are connected at the border of the box by periodic boundary conditions (PBC), as shown in Figure 2. In this way, the simulation box mimics the rigidity of an infinite (*n* units) oligomer $^3[^{\uparrow\uparrow}(Ru^{IV}\text{–}OH)(bda)_n@GS]^0$, as represented in Figure 1 and Figure 2. A separate DFT geometry optimization was performed to evaluate the stability of the system in the triplet spin state and total charge zero ($^3[^{\uparrow\uparrow}(Ru^{IV}\text{–}OH)(bda)_n@GS]^0$). The resulting geometry for the $^3[^{\uparrow\uparrow}(Ru^{IV}\text{–}OH)(bda)_n@GS]^0$ was then solvated with 50 water molecules, $^3[^{\uparrow\uparrow}(Ru^{IV}\text{–}OH)(bda)_n@GS]^0_{sol}$, corresponding to at least two solvation shells, as displayed by the radial distribution functions in Figure SI.1 in the Supporting Information, for a total amount of 259 atoms. In general, the

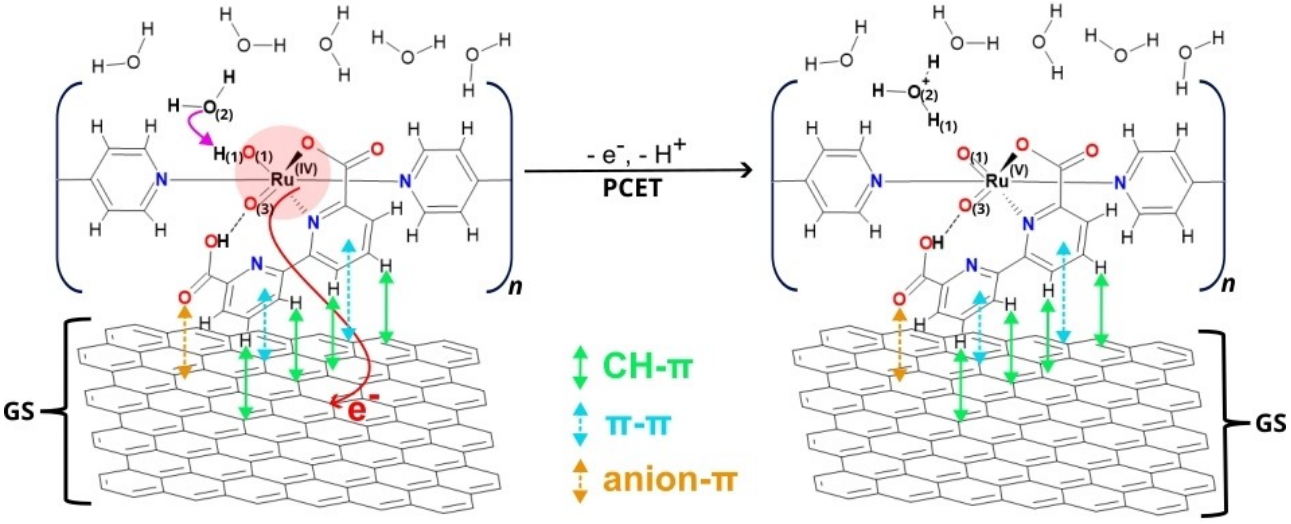

Figure 1. Illustrative bda-κ-NO configuration of the $Ru(bda)_n$ oligomeric chemical structures on a graphitic surface (GS) in a water environment during the PCET event. The proton transfer (PT) and electron transfer (ET) events from $(Ru^{IV}\text{–}OH)(bda)_n$ reactant state to $(Ru^{V}\text{=}O)(bda)_n$ product state are depicted by violet and red arrows, respectively. The oxygens and hydrogen involved in the PCET analysis are defined as $O_{(1)}$, $O_{(2)}$, $O_{(3)}$, and $H_{(1)}$, respectively. Schematic representation of possible anchoring noncovalent interactions: the main interaction CH-π in the green solid arrow, and the additional interactions π-π, and anion-π, in light blue, and orange dash arrows, respectively.

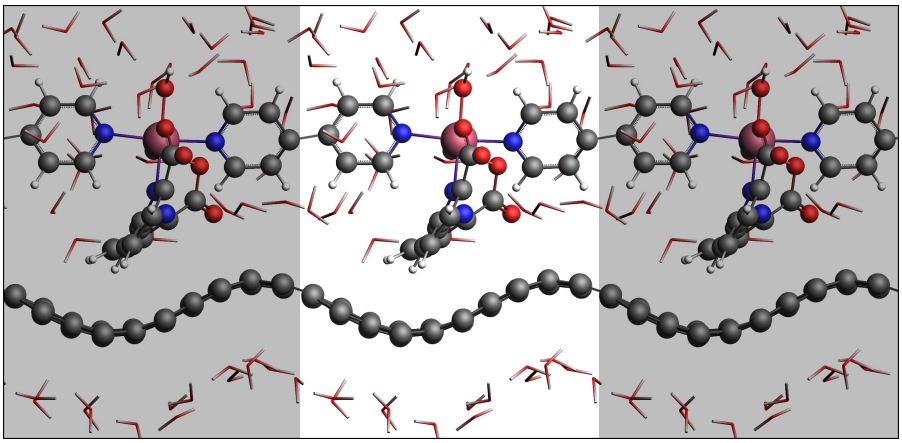

Figure 2. Snapshot of the $^{3}[^{\uparrow\uparrow}(Ru^{IV}–OH)(bda)_n@GS]^{0}_{sol}$ system in water after DFT-based MD equilibration (side view). In grey, the PBC images of the central simulation box provide the Ru(bda)$_n$ oligomer configuration anchored at the GS. In balls and sticks the (Ru^{IV}–OH)(bda)$_n$ and the GS, with ruthenium, carbon, oxygen, nitrogen, and hydrogen, in pink, grey, red, blue, and white colors, respectively. The water solvation is shown in sticks.

explicit solvation accounts for a proper description of the reaction path, activation energies, and the inclusion of the reorganization energy.[37–39] Subsequently, DFT-based MD NVE and NVT equilibration were performed, providing the initial configuration for the following DFT-based MD production runs, as depicted in Figure 2 (see Methods section).

Projected Density of States (PDOS) Analysis

On the equilibrated $^{3}[^{\uparrow\uparrow}(Ru^{IV}–OH)(bda)_n@GS]^{0}_{sol}$ geometry, the frontier electronic states have been explored via a Projected Density Of States (PDOS) analysis to estimate the energy gap for an efficient electron transfer (ET) during the PCET event. As reported in Figure 3a, the LUMO (dash bar) of the GS is higher ($\approx$3.0 eV) in energy than the HOMO (solid bar) of the (Ru^{IV}–OH)(bda)$_n$. With all the valence orbitals on the GS occupied, and the LUMO lying much higher in energy than the HOMO, there is no driving force for an ET event. Therefore, to mimic the influence of the experimentally applied electrode potential at the IV/V oxidation step,[30] and to make the ET event from the catalyst to the GS thermodynamically more feasible, we charged the GS surface positively creating an electron-acceptor hole. To estimate a realistic number of electrons to extract from the system, we used the following relation,

$$\Phi = \frac{\sigma}{C} + \Phi_{PZC} = \frac{ne}{CA} + \Phi_{PZC},$$

where Φ is the applied electrode potential, σ is the surface charge density, $e = 1.6 \times 10^{-19}$C is the elementary charge, C and Φ_{PZC} are the capacitance and potential of zero charge of the system (including the adsorbates), A is the surface area of the GS per computational cell, and n is the number of electrons

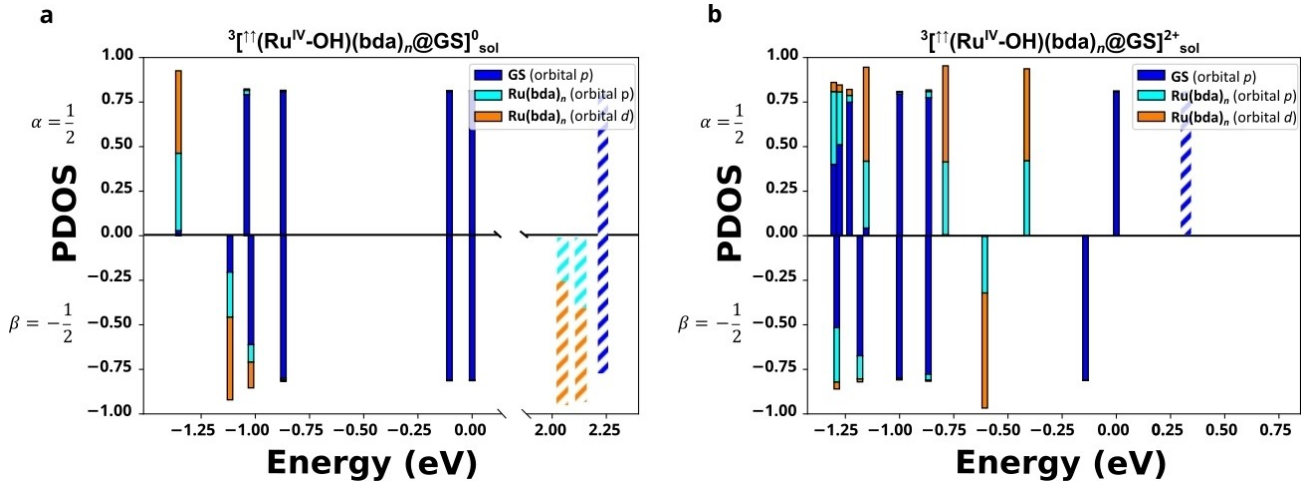

Figure 3. Projected Density of States (PDOS) for **a**, the DFT-based MD equilibrated configurations in water solvation of $^{3}[^{\uparrow\uparrow}(Ru^{IV}–OH)(bda)_n@GS]^{0}_{sol}$ and **b**, $^{3}[^{\uparrow\uparrow}(Ru^{IV}–OH)(bda)_n@GS]^{2+}_{sol}$. Solid and dash bars represent the occupied and empty orbitals, respectively. Blue color for the *p* orbital of GS and, orange and cyan colors for the *p* and *d* orbitals of Ru(bda)$_n$, respectively. The energy scale is set to 0.00 eV for the HOMO. The spin momentum is defined as $\pm^{1}/_{2}\hbar$ for electrons with spin up ($\uparrow = \alpha$) or down ($\downarrow = \beta$), respectively.

that should be extracted per computational cell. We approximated C and Φ_{PZC} based on the respective values obtained for pristine graphene. For C we used 21 μF/cm^2. For Φ_{PZC},[40] different values can be found in literature, ranging from −0.1 V *vs* SHE to +0.1 V *vs* SHE.[41–43] In this work we approximated it as 0 V *vs* SHE. Furthermore, we set A to the area of the simulation box (11.30×12.78 Å^2). Finally, for Φ we employed the experimental applied electrode potential at which the IV/V oxidation is experimentally found to occur at pH = 7.[30] This potential is given by $E_{exp(V/IV)} = 0.88$ V *vs* SHE (in the approximation NHE ≈ SHE).[30] Based on these values, we obtained $n = 1.7$. In order to extract full electrons, we set $n = 2$, leading to a system that has a total charge of 2+ (^{3}[$^{\uparrow\uparrow}$(Ru^{IV}–OH)(bda)$_n$@GS]$^{2+}{}_{sol}$). During each DFT-based simulation, the charge is compensated by a homogeneous background charge. Moreover, given the size of the simulation box and the electrostatic screening of the explicit water molecules, the possible spurious effect of periodic images is expected to be negligible.[44] The electronic structure of this doubly charged system is reported in Figure 3b. The energy gap between the HOMO of the (Ru^{IV}–OH)(bda)$_n$ and the LUMO of the GS is now ≈0.8 eV suggesting the presence of a barrier for the ET to occur (see Figure 3b). The catalyst $^{\uparrow\uparrow}$(Ru^{IV}–OH)(bda)$_n$ in a triplet spin state has the spin density mostly localized on the Ru and the O$_{(3)}$ (see Figure SI.2a in the Supporting Information and Figure 1 for nomenclature). For the whole system ^{3}[$^{\uparrow\uparrow}$(Ru^{IV}–OH)(bda)$_n$@GS]$^{2+}{}_{sol}$ both the α- and β-HOMO as well as the α-LUMO are delocalized over the GS (Figure 3b). Investigation of the activation free energy associated with the PCET event from the reactant state ^{3}[$^{\uparrow\uparrow}$(Ru^{IV}–OH)(bda)$_n$@GS]$^{2+}{}_{sol}$ to the product state ^{3}[(Ru^{V}=O)(bda)$_n$@GS]$^{+}{}_{sol}$ + H$^{+}{}_{sol}$ was conducted using DFT-based MD and the metadynamics enhanced sampling method.

DFT-Based MD Metadynamics for the PCET Event

After the initial equilibration and the extraction of two electrons from the GS, we conducted a 1.0 ps NVT DFT-based MD[45,46] metadynamics[47–49] simulation. This simulation aimed to capture the PCET event along a Collective Variable (CV) defined as the O$_{(1)}$–H$_{(1)}$ distance, where H$_{(1)}$ is the proton involved in the PT, as shown in Figure 1 and Figure 4a,b,e (see also Methods section). A free energy barrier $\Delta F \approx 1.2$ eV was found from the starting reactant system to the state when the proton was completely

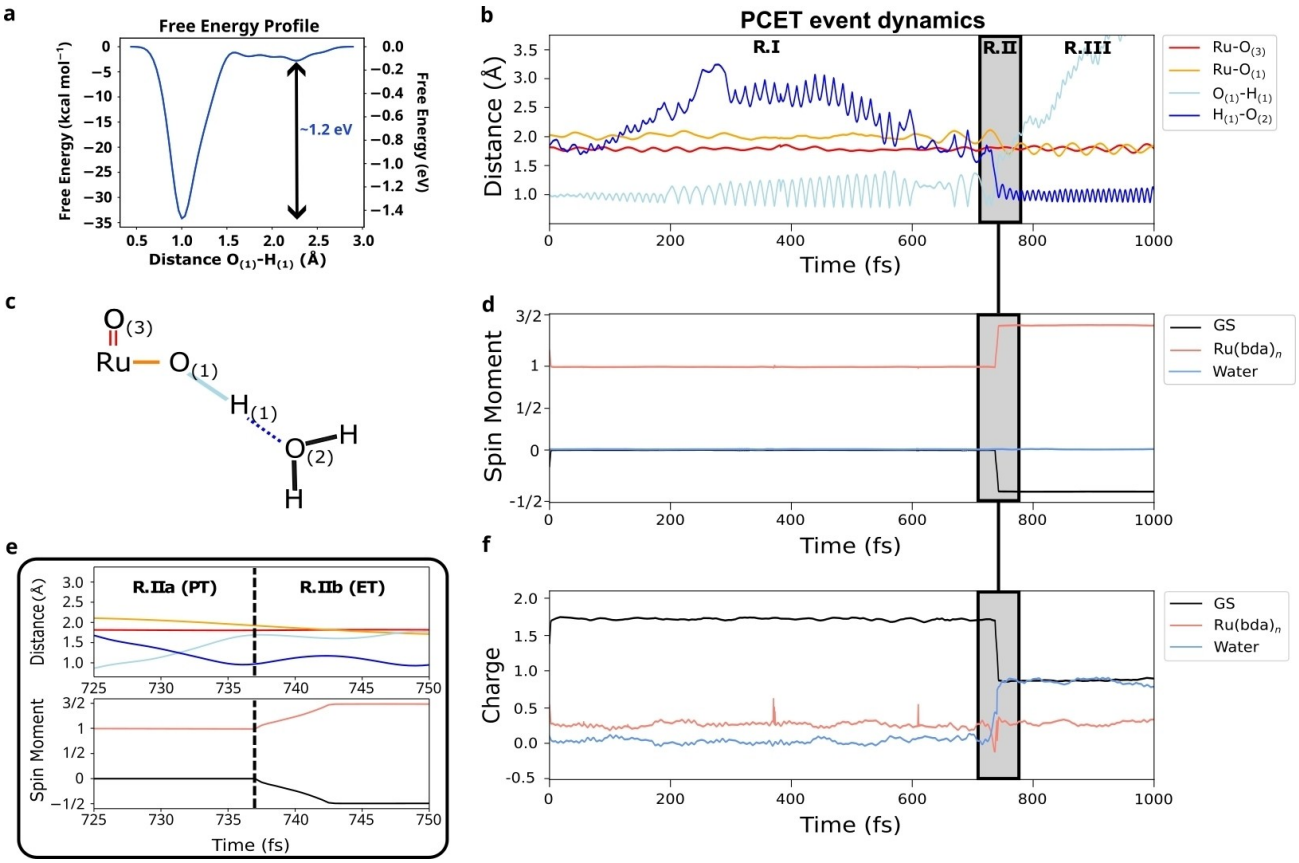

Figure 4. a, Free energy profile with free energy barrier of ≈1.2 eV (≈28 kcal mol^{-1}) along the Collective Variable (CV) O$_{(1)}$–H$_{(1)}$ (Å) over the 1.0 ps DFT-based MD metadynamics simulation. **b**, Time evolution (fs) of the Ru–O$_{(3)}$ (red line), Ru–O$_{(1)}$ (orange line), O$_{(1)}$–H$_{(1)}$ (light-blue line), and H$_{(1)}$–O$_{(2)}$ (blue line) bond distances (Å) during the PCET event (R.I, R.II, and R.III) described by the DFT-based MD metadynamics. **c**, Schematic representation of the bond distances analyzed, Ru–O$_{(3)}$ (red line), Ru–O$_{(1)}$ (orange line), O$_{(1)}$–H$_{(1)}$ (light-blue line) and H$_{(1)}$–O$_{(2)}$ (blue dash line). **d**, Time evolution (fs) of the spin moment of GS (black line), Ru(bda)$_n$ (red line), and water solvation (blue line) during the PCET event (R.I, R.II, and R.III). **e**, Enlargement of region R.II representing the PCET event with the time evolution (fs) of the Ru–O$_{(3)}$ (red line), Ru–O$_{(1)}$ (orange line), O$_{(1)}$–H$_{(1)}$ (light-blue line) and H$_{(1)}$–O$_{(2)}$ (blue line) bond distances (Å) and spin moment of GS (black line) and Ru(bda)$_n$ (red line). This region is further divided into R.IIa (PT) and R.IIb (ET). **f**, Time evolution (fs) of the Mulliken charges of GS (black line), Ru(bda)$_n$ (red line), and water solvation (blue line) during the PCET event (R.I, R.II, and R.III).

transferred to the first bulk water molecule (CV ≈ 2.3 Å), as shown in Figure 4a. Although the metadynamics does not appear to be fully converged due to insufficient sampling of the product state, the trajectory provides an insightful path for analyzing the PCET event and its representative configurations. A converged free energy surface (FES) would require a much longer metadynamics simulation and/or a different CV than the O–H distance. At the level of DFT used in this work (see Methods section), this simulation would result in an excessively high computational cost. During the DFT-based MD metadynamics simulation, the $O_{(1)}$–$H_{(1)}$ distance is observed to oscillate until the PCET event occurs and the system reaches the product state, $^{3}[(Ru^{V}{=}O)(bda)_n@GS]^{+}{}_{sol} + H^{+}{}_{sol}$ (Figure 4a,b). An analysis of the significant PCET distances along the trajectory (Figure 4c), reveals three key regions (Figure 4b). In the first part of the dynamics, reported as Region I (R.I) in Figure 4b, all the analyzed distances oscillate around their equilibrium values. Accordingly, the spin moments and Mulliken charges on $(Ru^{IV}{-}OH)(bda)_n$, GS, and water solvent also slightly oscillate for the whole R.I (Figure 4d,f). When the metadynamics bias potential reaches the peak of the free energy profile (Figure 4a), sharp changes in all the parameters along the trajectory are observed in Region II (R.II) (Figure 4b,d,f). The R.II has been characterized as the PCET region in Figure 4e and this can be further divided into two sub-regions, R.IIa and R.IIb, corresponding to the PT and ET steps, respectively (Figure 4e). Initially, the PT occurred (R.IIa) with the breaking of the $O_{(1)}$–$H_{(1)}$ bond (Figure 4b,c,e cyan line). Concomitantly, one of the water molecules in the first solvation shell gets the liberated proton (Figure 4b,c,e blue line) and the Ru–$O_{(1)}$ bond shortens to become a double bond in the oxidized system $(Ru^{V}{=}O)(bda)_n$ (Figure 4b,c,e orange line). The Ru=$O_{(3)}$ bond, intramolecularly coordinated with the hydrogen of the dangling carboxylic group of the bda ligand, remains unaltered (Figure 4b,c,e red line).[30] Then, in R.IIb a sharp change in the spin moment is noticeable, pointing out the occurrence of the ET step (Figure 4d,e). The R.II displays a change in the Mulliken charges with the GS that gains one electron and shifts from charge ≈2+ to ≈1+ (Figure 4f). The total Mulliken charge on the $Ru(bda)_n$ oligomer catalyst stays constant because it is oxidized to $(Ru^{V}{=}O)(bda)_n$ donating an electron to the GS and at the same time donating a proton to the water solvation bulk with the formation of a hydronium ion (Figure 4f) and a double bond Ru=$O_{(1)}$ (Figure 4b orange line). Region III (R.III) addresses the product state $(Ru^{V}{=}O)(bda)_n$ where there are three unpaired electrons of spin up on the $(Ru^{V}{=}O)(bda)_n$, S = 3/2 (quartet spin state), and one unpaired electron of spin down on the GS, S = −1/2 (doublet spin state), while the total multiplicity in the system (2S + 1 = 3) is conserved along the PCET reaction.

The PDOS of two representative configurations in R.IIa and R.IIb, respectively, are reported in Figure 5a,b. When the DFT-based MD metadynamics has reached the PT event in the region R.IIa of the trajectory, the HOMO (Figure SI.3a in the Supporting Information) of the $(Ru^{IV}{-}OH)(bda)_n$ is ≈0.1 eV higher in energy than the LUMO of the GS, establishing an electronic driving force for the ET event (Figure 5a). This seemingly non-aufbau result arises from the fact that in the PDOS analysis of a selected configuration, a starting bias on the electronic configuration is used corresponding to the initial diabatic state with the electron still on the catalyst (reactant state). The close proximity of the HOMO and LUMO characterizes a scenario that can be related to an intersection region between the two diabatic states. In R.IIb, the PDOS reveals that a crossing of eigenvalues has occurred: the HOMO of the $(Ru^{IV}{-}OH)(bda)_n$ has transitioned to become the LUMO of $(Ru^{V}{=}O)(bda)_n$, and *vice versa*, the LUMO of GS has been filled with the transferred electron, resulting in the GS HOMO and confirming the occurrence of the ET step, as displayed in Figure 5b and Figure SI.3b in the Supporting Information. After the PCET event, in region R.III, the catalyst exhibits a quartet spin state $^{\uparrow\uparrow\uparrow}(Ru^{V}{=}O)(bda)_n$ with three singly occupied MOs and

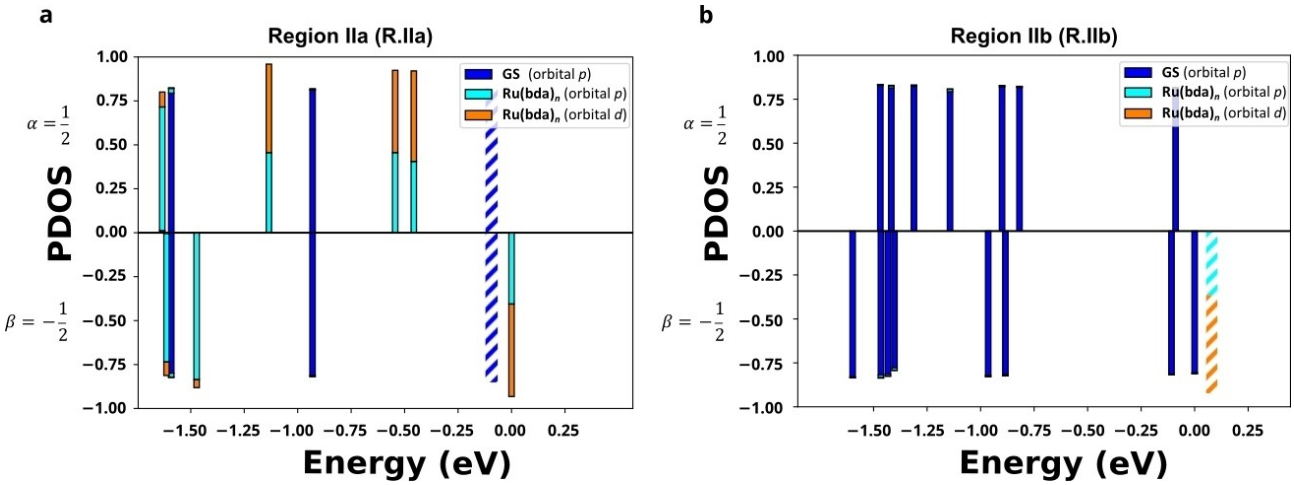

Figure 5. Projected Density of States (PDOS) for two configurations of $Ru(bda)_n$@GS from the DFT-based MD metadynamics **a**, in region R.IIa (PT) and **b**, in region R.IIb (ET). Solid and dash bars represent occupied and empty states, respectively. Blue color for the *p* orbital of GS and, orange and cyan colors for the *p* and *d* orbitals of $Ru(bda)_n$, respectively. The energy scale is set to 0.00 eV for the HOMO. The spin momentum is defined as $\pm^{1}/_{2}\hbar$ for electrons with spin up (↑ = α) or down (↓ = β), respectively.

a spin density delocalized over the Ru, $O_{(3)}$, and $O_{(1)}$ (see Figure SI.4 in the Supporting Information).

Quartet or Doublet Spin State for the Product (Ru^{V}=O)(bda)$_n$

The catalyst spin state, hereafter indicated in bold characters, for the product (Ru^{V}=O)(bda)$_n$ of the PCET step was determined to be a quartet within an overall triplet spin state complex, $^{3}[^{\uparrow\uparrow\uparrow}$**($Ru^{V}$=O)(bda)$_n$**@$^{\downarrow}GS]^{+}_{sol} + H^{+}_{sol}$. However, EPR experiments conducted by Gil-Sepulcre et al. on the (Ru^{V}=O)(bda)$_n$ oligomeric product anchored at the graphitic surface identified a doublet spin state.[30] Consequently, the energetics of both the quartet ($^{\uparrow\uparrow\uparrow}$**($Ru^{V}$=O)(bda)$_n$**) and doublet ($^{\uparrow}$**($Ru^{V}$=O)(bda)$_n$**) spin states of the ($Ru^{V}$=O)(bda)$_n$ product complex have been investigated and compared to the reactant triplet spin state ($^{\uparrow\uparrow}$**(Ru^{IV}–OH)(bda)$_n$**). Initially, a 2.0 ps NVT DFT-based MD equilibration was conducted for the reactant triplet spin state ($^{3}[^{\uparrow\uparrow}$**(Ru^{IV}–OH)(bda)$_n$**@GS$]^{2+}_{sol}$) to be taken as reference for the energetics analysis of the product spin states. Subsequently, other two separate 2.0 ps NVT DFT-based MD equilibrations were carried out for the possible product systems with the catalyst in the quartet spin state ($^{3}[^{\uparrow\uparrow\uparrow}$**($Ru^{V}$=O)(bda)$_n$**@$^{\downarrow}GS]^{+}_{sol} + H^{+}_{sol}$) and in the doublet spin state ($^{1}[^{\uparrow}$**(Ru^{V}=O)(bda)$_n$**@$^{\downarrow}$GS$]^{+}_{sol} + H^{+}_{sol}$), respectively. The simulations for the products, quartet and doublet spin states, were initiated from a snapshot in Region III of the product quartet spin state $^{3}[^{\uparrow\uparrow\uparrow}$**($Ru^{V}$=O)(bda)$_n$**@$^{\downarrow}GS]^{+}_{sol} + H^{+}_{sol}$. The initial geometry of the doublet spin state was obtained by manually spin flipping one electron from the $^{\uparrow\uparrow\uparrow}$**($Ru^{V}$=O)(bda)$_n$** geometry to form $^{\uparrow}$**(Ru^{V}=O)(bda)$_n$**. The MOs representation of the product doublet spin state $^{\uparrow}$**(Ru^{V}=O)(bda)$_n$** is reported in Figure SI.5a,b in the Supporting Information. We also considered the doublet spin state case in which the unpaired electron on the catalyst has the same spin as the unpaired electron on the GS, $^{3}[^{\uparrow}$**(Ru^{V}=O)(bda)$_n$**@$^{\uparrow}$GS$]^{+}_{sol} + H^{+}_{sol}$. However, this system turned out to be unstable according to our 2.0 ps NVT DFT-based MD equilibration and was not further considered in the analysis (see Figure SI.6 in the Supporting Information). The cumulative averages of Kohn-Sham (KS) potential energies of the reactant triplet spin state ($^{3}[^{\uparrow\uparrow}$**(Ru^{IV}–OH)(bda)$_n$**@GS$]^{2+}_{sol}$) and product spin states, quartet $^{3}[^{\uparrow\uparrow\uparrow}$**($Ru^{V}$=O)(bda)$_n$**@$^{\downarrow}GS]^{+}_{sol} + H^{+}_{sol}$) and doublet $^{1}[^{\uparrow}$**(Ru^{V}=O)(bda)$_n$**@$^{\downarrow}$GS$]^{+}_{sol} + H^{+}_{sol}$), respectively, are reported in Figure 6 (the corresponding KS potential energy fluctuations are shown in Figure SI.7). The cumulative averages of the KS potential energies are computed starting after the first 0.4 ps of each NVT DFT-based MD, where the initial relaxation occurs. The product quartet spin state results comparable in energy to the reactant triplet spin state (Figure 6). Instead, the product doublet spin state is ≈0.36 eV lower than the product quartet spin state.

To determine constant potential reaction energetics the first-order correction to capacitive charging was employed on the KS potential energies.[50,51] We refer to the Methods section for the definition of this correction. This correction approach enables a comparison between KS potential energies, and more extensively the electrochemical reaction energetics, at constant potential of the reactant (R) in the triplet spin state ($^{3}[^{\uparrow\uparrow}$**(Ru^{IV}–OH)(bda)$_n$**@GS$]^{2+}_{sol}$), and product (P) in the quartet ($^{3}[^{\uparrow\uparrow\uparrow}$**($Ru^{V}$=O)(bda)$_n$**@$^{\downarrow}GS]^{+}_{sol} + H^{+}_{sol}$) and doublet ($^{1}[^{\uparrow}$**($Ru^{V}$=O)(bda)$_n$**@$^{\downarrow}GS]^{+}_{sol} + H^{+}_{sol}$) spin states. Table 1 presents the computed corrections on the products in quartet and doublet spin states, relative to the reactant triplet spin state ($^{3}[^{\uparrow\uparrow}$**(Ru^{IV}–OH)(bda)$_n$**@GS$]^{2+}_{sol}$). This correction led to a shift of $\Delta E_{corr} - \Delta E = -0.11$ eV for the quartet spin state ($^{3}[^{\uparrow\uparrow\uparrow}$**($Ru^{V}$=O)(bda)$_n$**@$^{\downarrow}GS]^{+}_{sol} + H^{+}_{sol}$) and $\Delta E_{corr} - \Delta E = -0.09$ eV

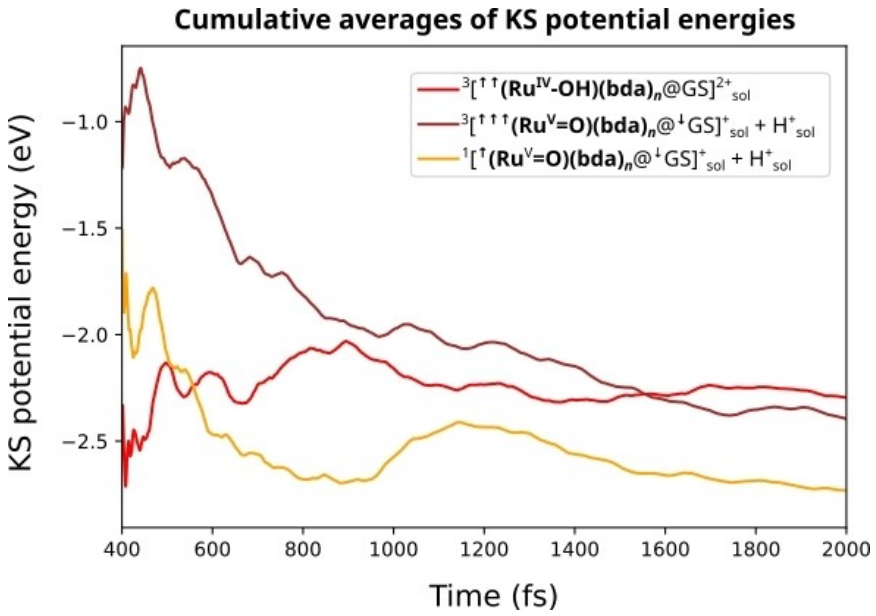

Figure 6. Cumulative averages of KS potential energies (eV) fluctuations from 0.4 ps to 2.0 ps of each NVT DFT-based MD equilibration. The red line represents the reactant triplet spin state system ($^{3}[^{\uparrow\uparrow}$**(Ru^{IV}–OH)(bda)$_n$**@GS$]^{2+}_{sol}$), while the brown and yellow lines correspond to the products, $^{3}[^{\uparrow\uparrow\uparrow}$**($Ru^{V}$=O)(bda)$_n$**@$^{\downarrow}GS]^{+}_{sol} + H^{+}_{sol}$ and $^{1}[^{\uparrow}$**(Ru^{V}=O)(bda)$_n$**@$^{\downarrow}$GS$]^{+}_{sol} + H^{+}_{sol}$, with the catalyst in the quartet and doublet spin state, respectively.

Table 1. Changes for the products quartet and doublet spin states, $^3[^{\uparrow\uparrow\uparrow}$**(Ru^{V}=O)(bda)**$_n$**@$^{\downarrow}$GS]$^{+}_{sol}$** $+ H^{+}_{sol}$ and $^1[^{\uparrow}$**(Ru^{V}=O)(bda)**$_n$**@$^{\downarrow}$GS]$^{+}_{sol}$** $+ H^{+}_{sol}$, relative to the reactant triplet spin state, $^3[^{\uparrow\uparrow}$**(Ru^{IV}–OH)(bda)**$_n$**@GS]$^{2+}_{sol}$**, denoted as P and R in the first order correction to capacitive charging, respectively (see Methods section).[50,51] The table includes changes in system KS potential energies ($\Delta E = E_P(\Phi_P) - E_R(\Phi_R)$), GS Mulliken charges ($q_P - q_R$), system work functions ($\Phi_P - \Phi_R$) approximated to each system HOMO level, and corrected system KS potential energies at constant potential ($\Delta E_{corr} = E_P(\Phi_R) - E_R(\Phi_R)$). All values for ΔE and Φ are listed in eV, q is given in atomic units *e*.

Product (P)	ΔE (eV)	$q_P - q_R$	$\Phi_P - \Phi_R$ (eV)	ΔE_{corr} (eV)
$^3[^{\uparrow\uparrow\uparrow}$(Ru^{V}=O)(bda)$_n$@$^{\downarrow}$GS]$^{+}_{sol}$ $+ H^{+}_{sol}$	−0.08	0.55	−0.42	−0.19
$^1[^{\uparrow}$(Ru^{V}=O)(bda)$_n$@$^{\downarrow}$GS]$^{+}_{sol}$ $+ H^{+}_{sol}$	−0.46	0.53	−0.36	−0.55

for the doublet spin state ($^1[^{\uparrow}$**(Ru^{V}=O)(bda)**$_n$**@$^{\downarrow}$GS]$^{+}_{sol}$** $+ H^{+}_{sol}$), respectively, compared to the reactant triplet spin state. The product doublet spin state is found to be lower in KS potential energy than the reactant triplet spin state. The product quartet spin state remains higher in energy compared to the doublet spin state and slightly lower than the triplet spin state. This fact is in line with the initial hypothesis that removing two electrons from the GS would correspond to the experimentally applied potential, thus making this reaction energetically viable. The thermodynamic stability of the product doublet spin state suggests that the quartet spin state observed during the DFT-based MD metadynamics is an intermediate that can possibly decay via intersystem crossing to the experimentally more stable doublet spin state.[30]

Dynamical Effect of the CH-π Stacking Anchoring on the PCET Event

DFT-based MD is the ideal approach to analyze possible dynamical effects of the CH-π stacking anchoring between $^3[^{\uparrow\uparrow}$**(Ru^{IV}–OH)(bda)**$_n$**@GS]$^{2+}_{sol}$** and the GS on the PCET event, as it allows for the monitoring of charge fluctuations and nuclear vibrational motions at the same time.[52,53] Therefore, the separate 2.0 ps NVT DFT-based MD trajectories on the reactant triplet spin state ($^3[^{\uparrow\uparrow}$**(Ru^{IV}–OH)(bda)**$_n$**@GS]$^{2+}_{sol}$**), and the products, quartet spin state ($^3[^{\uparrow\uparrow\uparrow}$**(Ru^{V}=O)(bda)**$_n$**@$^{\downarrow}$GS]$^{+}_{sol}$** $+ H^{+}_{sol}$) and doublet spin state ($^1[^{\uparrow}$**(Ru^{V}=O)(bda)**$_n$**@$^{\downarrow}$GS]$^{+}_{sol}$** $+ H^{+}_{sol}$), were used to perform a Vibrational Density of States (VDOS) analysis.[52,53] The geometrical parameters followed along the trajectory (from 0.4 ps to 2.0 ps) are the distances between the four interacting hydrogen atoms of the bda ligand and four centers of mass of the closest six carbons rings on the GS ($H_{(1bda)}$–$GS_{(com1)}$, $H_{(2bda)}$–$GS_{(com2)}$, $H_{(3bda)}$–$GS_{(com3)}$, $H_{(4bda)}$–$GS_{(com4)}$) involved in the CH-π stacking, the Ru–$O_{(1)}$ bond distance, the $O_{(1)}$–$H_{(1)}$ bond distance (for the (Ru^{IV}–OH)(bda)$_n$ case only), as depicted in Figure 7a. Furthermore, we follow the Mulliken charges fluctuations along the dynamics on the GS, and on the Ru and $O_{(1)}$ atoms of the Ru^{IV}(bda)$_n$ and (Ru^{V}=O)(bda)$_n$. A gaussian window function with a sigma value of 15 was chosen for each VDOS analysis. The time evolutions of the investigated CH-π stacking anchoring distances, Ru–$O_{(1)}$ and $O_{(1)}$–$H_{(1)}$ bond distances, and Mulliken charges on the GS, the Ru and $O_{(1)}$ atoms, along each NVT DFT-based MD, are reported in Figures SI.8a,b,c, SI.9a,b,c, SI.10a,b,c, in the Supporting Information, respectively. Notably, the stability of the Ru(bda)$_n$ oligomeric system is confirmed by the small fluctuations observed in each selected CH-π stacking distance, as reported in Figure SI.8 in the Supporting Information. The rationale for choosing these parameters is to address the nuclear modes involved in the CH-π stacking anchoring, in the oxidation of the triplet spin state to the quartet or doublet spin states, and to search for possible correlations with characteristic frequencies in the electron charge fluctuations during the PCET event. The VDOS analysis allows exploring possible vibronic couplings present in our adiabatic DFT-based scheme description of the PCET process.[54] The VDOS of both reactant and product states in Figure 7b,c,d exhibit resonances in the range of 800–1000 cm^{-1} (0.1–0.12 eV) between the frequencies associated to GS Mulliken charge fluctuations and those related to CH-π stacking anchoring distances $H_{(1bda)}$–$GS_{(com1)}$, $H_{(2bda)}$–$GS_{(com2)}$, $H_{(3bda)}$–$GS_{(com3)}$, $H_{(4bda)}$–$GS_{(com4)}$ and Ru–$O_{(1)}$ bond distance (Figure 7b,c,d insets). The observed resonances in the region of 800–1000 cm^{-1} (0.1–0.12 eV) for both reactant and product cases are supposed to facilitate the ET step. Other resonances between the same parameters are present in the range of 3000–3200 cm^{-1} characteristic of aromatic C–H and O–H stretching modes (Figure 7b,c,d insets). Interestingly, in this range of frequencies, a correlation is found between the oscillations of Mulliken charges in the Ru–$O_{(1)}$ and the GS. In summary, the dynamics of the CH-π stacking anchoring as well as that of Ru–$O_{(1)}$ and $O_{(1)}$–$H_{(1)}$ bonds strongly couple with the Mulliken charge fluctuations on the GS and on the Ru and $O_{(1)}$. These dynamic interactions connect every element, from the leaving proton and the catalyst to the GS, and play a crucial role in stabilizing the anchoring and fostering possible vibronic couplings during the PCET event dynamics.[52,53]

Conclusions

This work explores at the DFT-based MD level the dynamics of the PCET event in the following catalytic reaction of the Ru(bda)$_n$ oligomer anchored to a graphitic surface (GS):

$$^3[^{\uparrow\uparrow}(\mathbf{Ru^{IV}-OH})(\mathbf{bda})_n@GS]^{2+}_{sol} \xrightarrow{-e^-,-H^+} [(Ru^{V}{=}O)(bda)_n@GS]^{+} + H^{+}_{sol}.$$

The CH-π stacking anchoring has been experimentally reported as a novel way to stabilize the catalyst on the graphitic surface by Gil-Sepulcre et al.[30] The computationally obtained product quartet spin state ($^3[^{\uparrow\uparrow\uparrow}$**(Ru^{V}=O)(bda)**$_n$**@$^{\downarrow}$GS]$^{+}_{sol}$** $+ H^{+}_{sol}$) has been compared to the doublet spin state ($^1[^{\uparrow}$**(Ru^{V}=O)(bda)**$_n$**@$^{\downarrow}$GS]$^{+}_{sol}$** $+ H^{+}_{sol}$) expected experimentally by Gil-Sepulcre et al.[30] After applying the first-order correction to capacitive charging for constant potential energetics analysis,[50,51] we found that the KS potential energy of the

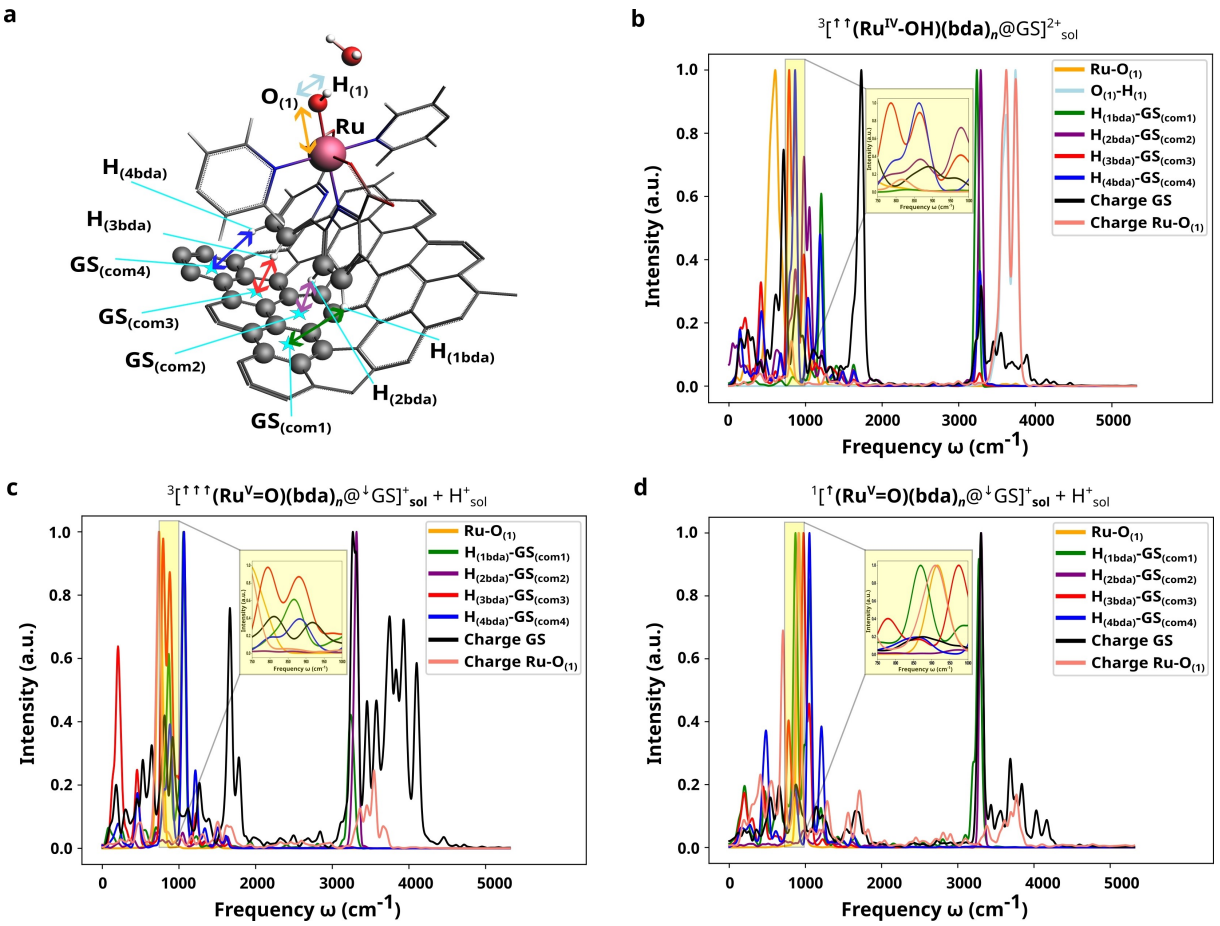

Figure 7. a, Schematic representation of $^{3}[^{\uparrow\uparrow}(Ru^{IV}–OH)(bda)_n@GS]^{2+}{}_{sol}$ system and the bond distances parameters investigated via VDOS, Ru–$O_{(1)}$, $O_{(1)}$–$H_{(1)}$, $H_{(1bda)}$–$GS_{(com1)}$, $H_{(2bda)}$–$GS_{(com2)}$, $H_{(3bda)}$–$GS_{(com3)}$, and $H_{(4bda)}$–$GS_{(com4)}$, in dark yellow, light blue, green, violet, red, and blue arrows, respectively. The hydrogens of the bda ligand and the centers of mass (com) on the GS involved in the CH-stacking are indicated with cyan sticks and stars, respectively. Besides the proton acceptor water molecule, the rest of the water solvation molecules are omitted for clarity. **b**, VDOS *vs* frequencies ω (cm^{-1}) of the distance parameters, Ru–$O_{(1)}$, $O_{(1)}$–$H_{(1)}$, $H_{(1bda)}$–$GS_{(com1)}$, $H_{(2bda)}$–$GS_{(com2)}$, $H_{(3bda)}$–$GS_{(com3)}$, and $H_{(4bda)}$–$GS_{(com4)}$, in dark yellow, light blue, green, violet, red, and blue lines, respectively, and of the Mulliken charges on GS and Ru–$O_{(1)}$ in black and orange lines, respectively, in the separate NVT DFT-based MD on the triplet spin state reactant system $^{3}[^{\uparrow\uparrow}(Ru^{IV}–OH)(bda)_n@GS]^{2+}{}_{sol}$. **c**,**d**, VDOS *vs* frequencies ω (cm^{-1}) of the distance parameters, Ru–$O_{(1)}$, $H_{(1bda)}$-$GS_{(com1)}$, $H_{(2bda)}$-$GS_{(com2)}$, $H_{(3bda)}$-$GS_{(com3)}$, and $H_{(4bda)}$-$GS_{(com4)}$, in dark yellow, green, violet, red, and blue lines, respectively, and of the Mulliken charges on GS and Ru–$O_{(1)}$ in black and orange lines, respectively, in the separate NVT DFT-based MDs on the products, quartet spin state $^{3}[^{\uparrow\uparrow\uparrow}(Ru^{V}=O)(bda)_n@GS]^{+}{}_{sol} + H^{+}{}_{sol}$ and the doublet spin state $^{3}[^{\uparrow}(Ru^{V}=O)(bda)_n@GS]^{+}{}_{sol} + H^{+}{}_{sol}$, respectively. Yellow insets in **b**, **c**, and **d**, magnify the VDOS in the range of 750–1000 cm^{-1} where relevant resonances can be observed.

product doublet spin state is lower than that of both the product quartet spin state and the reactant triplet spin state. Moreover, the product quartet spin state is slightly more stable than the reactant triplet spin state. These findings can suggest the presence of a short-lived catalytic intermediate quartet spin state that may decay via intersystem crossing to the observed and thermodynamically more stable doublet spin state.[30] The stability of the Ru(bda)$_n$ oligomeric system on the GS is validated through the small fluctuations observed in the CH-π stacking distances. Finally, the VDOS analysis of the DFT-based MD trajectories reveals a possible vibronic coupling between the CH-π stacking anchoring distances, Ru–$O_{(1)}$ and $O_{(1)}$–$H_{(1)}$ bond distances, and the Mulliken charge fluctuations of the GS and the Ru and $O_{(1)}$ on the catalyst. The discovered resonances establish correlations among each element of the PCET event under investigation: the water bulk, the catalyst, and the graphitic surface. These insights offer a deeper understanding of the PCET mechanism of the Ru(bda)$_n$ oligomer anchored to a graphitic surface, serving as a water oxidation molecular anode.

Methods

Preliminary DFT-Based Static Calculations

The DFT-based geometry optimizations were performed using the CP2K code[46] with the B3LYP hybrid functional,[55–58] D3(BJ) atom-pairwise dispersion corrections,[59,60] and double-zeta basis set with one additional set of polarization functions (DZVP-MOLOPT-SR-GTH for ruthenium and DZVP-MOLOPT-GTH for the other elements) was chosen in accordance with previous literature for similar catalytic systems.[35,61] The Auxiliary-Density-Matrix Methods (ADMM) was employed in the calculations (see Supporting Information for the input files).[62] First the initial state of the $^{3}[^{\uparrow\uparrow}(Ru^{IV}–OH)(bda)_1]^{0}$ monomeric catalyst was

optimized and then the $^{3}[^{\uparrow\uparrow}(Ru^{IV}–OH)(bda)_n@GS]^{0}$ oligomeric molecular system including an amount of 50 explicit water molecules in a MD box of dimensions 11.30×12.78×16.00 Å^3 was optimized, resulting in the optimized $^{3}[^{\uparrow\uparrow}(Ru^{IV}–OH)(bda)_n@GS]^{0}{}_{sol}$ molecular system. This last optimized geometry was subsequently used as a starting configuration for the first DFT-based MD runs, NVE and NVT (before the extraction of two electrons).

DFT-Based MDs and Metadynamics

The DFT-based MD simulations were carried out using periodic boundary conditions (PBC) and with the hybrid Gaussian and plane wave approach,[63] as implemented in the CP2K/Quickstep code.[46] The Kohn-Sham orbitals were described by an accurate molecularly optimized double-zeta basis set with one additional set of polarization functions (DZVP-MOLOPT-SR-GTH for ruthenium and DZVP-MOLOPT-GTH for the other elements), while the charge density was represented by plane waves with a density cutoff of 600 Ry.[61] Separable norm-conserving pseudopotentials were used to mimic the interactions between the valence electrons and the ionic cores.[64,65] The B3LYP hybrid functional was employed since it was shown to be well-accurate in describing transition-metal complexes, including Ru-based WOCs.[30,66,67] The damped D3(BJ) atom-pairwise dispersion correction was added to account for long-range van der Waals interactions.[59,60] For the NVT before the extraction of two electrons and all production NVT DFT-based MD simulations, a Nosé-Hoover chains (NHC) thermostat was used, with a length of the Nose-Hoover chain and time constant of the thermostat chain of 7 and 10 fs, respectively. For the NVE and NVT before the extraction of two electrons and production NVT DFT-based MD simulations, the time step and temperature were 0.5 fs and 300 K, respectively. To compute the net atomic charges, the Mulliken population was used.[68] The PDOS analysis was conducted on selected configurations using the corresponding CP2 K code analysis tool.[46] Therefore, starting from the previous geometry optimized $^{3}[^{\uparrow\uparrow}\mathbf{(Ru^{IV}–OH)(bda)}_n@GS]^{0}{}_{sol}$ molecular system, 0.5 ps of NVE DFT-based MD and then other 0.5 ps of NVT DFT-based MD were executed. After the extraction of two electrons from the last equilibrated geometry, 1.0 ps of NVT DFT-based MD metadynamics production run was conducted on $^{3}[^{\uparrow\uparrow}\mathbf{(Ru^{IV}–OH)(bda)}_n@GS]^{2+}{}_{sol}$ to describe the PCET event. The DFT-based MD metadynamics is performed employing the PLUMED plugin[69] with width = 0.1 Å, height = 1.0 kJ mol^{-1}, and deposition frequency of Gaussian hills every 25 time steps.[47] Subsequently, 2.0 ps of NVT DFT-based MD equilibrations were conducted separately for the system with the catalyst in the reactant triplet spin state ($^{3}[^{\uparrow\uparrow}\mathbf{(Ru^{IV}–OH)(bda)}_n@GS]^{2+}{}_{sol}$), and in the products, quartet ($^{3}[^{\uparrow\uparrow\uparrow}\mathbf{(Ru^{V}=O)(bda)}_n@^{\downarrow}GS]^{+}{}_{sol} + H^{+}{}_{sol}$) and doublet ($^{1}[^{\uparrow}\mathbf{(Ru^{V}=O)(bda)}_n@^{\downarrow}GS]^{+}{}_{sol} + H^{+}{}_{sol}$) spin states, respectively. The Auxiliary-Density-Matrix Methods (ADMM) was employed in the calculations (see Supporting Information for the input files).[62] Representative input files for the DFT-based equilibrations and metadynamics are reported in Supporting Information.

Constant Potential Reaction Energetics Correction

The method used to determine constant potential reaction energetics required only a single barrier calculation and the corresponding electrode charge, *i.e.* graphitic surface (GS) charge, in accordance with the work by Chan and Nørskov.[50,51] This first-order correction to capacitive charging is grounded in the premise that the energies associated with electron transfer across interfaces can be distinctly separated into contributions from chemical and electrostatic factors.[50,51] The electrostatic contribution to the energy change can be expressed purely in terms of capacitance.[50,51] This analysis was conducted at both the reactant (R) state ($^{3}[^{\uparrow\uparrow}\mathbf{(Ru^{IV}–OH)(bda)}_n@GS]^{2+}{}_{sol}$) and product (P) states ($^{3}[^{\uparrow\uparrow\uparrow}\mathbf{(Ru^{V}=O)(bda)}_n@^{\downarrow}GS]^{+}{}_{sol} + H^{+}{}_{sol}$ and $^{1}[^{\uparrow}\mathbf{(Ru^{V}=O)(bda)}_n@^{\downarrow}GS]^{+}{}_{sol} + H^{+}{}_{sol}$).[50,51] For a given PCET event from reactant state R to the product state P, the total energy change in the simulation cell at constant potential with the respect to the reactant (R) is described by

$$E_P(U_R) - E_R(U_R) = [E_P(U_P) - E_R(U_R)] + \frac{e(q_P - q_R)(U_P - U_R)}{2},$$

where the first term on the right refers to the electrostatic contribution to the energy change between states R and P at different potentials U_R and U_P, respectively, in the second term, $q_P - q_R$ is the change on the GS charge from state R to P, and the term $(U_P - U_R)/2$ gives the finite cell contribution.[50,51] This equation can be rewritten in terms of work functions Φ_i according to

$$E_P(\Phi_R) - E_R(\Phi_R) = [E_P(\Phi_P) - E_R(\Phi_R)] + \frac{(q_P - q_R)(\Phi_P - \Phi_R)}{2},$$

where the first term on the right side describes the difference of the KS potential energies of the product state and reactant states, P and R, respectively, and the second term $q_P - q_R$ can be estimated from the Mulliken charge analysis on the GS before and after the electron transfer event (ET).[50,51] Each work functions Φ_i is set equal to the HOMO energy of state *i*, which are the product or reactant states, P or R, respectively. In this work each term of the upper equation was extrapolated from the average on twenty DFT-based single point calculations extracted every 20 fs along the last 0.4 ps of each independent NVT DFT-based MD equilibration on the reactant triplet spin state R ($^{3}[^{\uparrow\uparrow}\mathbf{(Ru^{IV}–OH)(bda)}_n@GS]^{2+}{}_{sol}$) and product quartet and doublet spin states P, ($^{3}[^{\uparrow\uparrow\uparrow}\mathbf{(Ru^{V}=O)(bda)}_n@^{\downarrow}GS]^{+}{}_{sol} + H^{+}{}_{sol}$ and $^{1}[^{\uparrow}\mathbf{(Ru^{V}=O)(bda)}_n@^{\downarrow}GS]^{+}{}_{sol} + H^{+}{}_{sol}$), respectively. All the DFT-based single points were performed using the CP2 K code[46] with the B3LYP hybrid functional,[55–58] D3(BJ) atom-pairwise dispersion corrections[59,60] and double-zeta basis set with one additional set of polarization functions (DZVP-MOLOPT-SR-GTH for Ruthenium and DZVP-MOLOPT-GTH for the other elements). The Auxiliary-Density-Matrix Methods (ADMM) was employed in the calculations (see Supporting Information for the input files).[62]

Supporting Information

The authors have cited additional references within the Supporting Information.[70] The Supporting Information includes additional computational analysis, DFT-based input files for geometry optimization, NVE MD, NVT MD equilibration, and NVT MD metadynamics, and DFT-based optimized and representative DFT-based NVT equilibrated geometries.

Acknowledgements

This work was sponsored by NWO – Domain Science for the use of supercomputer facilities. We acknowledge Dr. Katharina Doblhoff-Dier for the fruitful discussions and suggestions during this work.

Conflict of Interests

The authors declare no conflict of interest.

Data Availability Statement

The data that support the findings of this study are available from the corresponding author upon request.

Keywords: DFT-based Molecular Dynamics · Metadynamics · Proton-Coupled Electron Transfer · Vibrational Resonances · Water Oxidation Catalysis

[1] J. D. Blakemore, R. H. Crabtree, G. W. Brudvig, *Chem. Rev.* **2015**, *115*, 12974–13005.
[2] S. Berardi, S. Drouet, L. Francàs, C. Gimbert-Suriñach, M. Guttentag, C. Richmond, T. Stoll, A. Llobet, *Chem. Soc. Rev.* **2014**, *43*, 7501–7519.
[3] P. Garrido-Barros, C. Gimbert-Suriñach, R. Matheu, X. Sala, A. Llobet, *Chem. Soc. Rev.* **2017**, *46*, 6088–6098.
[4] R. Matheu, P. Garrido-Barros, M. Gil-Sepulcre, M. Z. Ertem, X. Sala, C. Gimbert-Suriñach, A. Llobet, *Nat. Chem. Rev.* **2019**, *3*, 331–341.
[5] R. Matheu, M. Z. Ertem, C. Gimbert-Suriñach, X. Sala, A. Llobet, *Chem. Rev.* **2019**, *119*, 3453–3471.
[6] J. Xu, S. Murphy, D. Xiong, R. Cai, X.-K. Wei, M. Heggen, E. Barborini, S. Vinati, R. E. Dunin-Borkowski, R. E. Palmer, L. Liu, *ACS Appl. Energ. Mater.* **2018**, *1*, 3013–3018.
[7] W. Li, X. Gao, X. Wang, D. Xiong, P.-P. Huang, W.-G. Song, X. Bao, L. Liu, *J. Power Sources* **2016**, *330*, 156–166.
[8] L. Francàs, C. Richmond, P. Garrido-Barros, N. Planas, S. Roeser, J. Benet-Buchholz, L. Escriche, X. Sala, A. Llobet, *Chem. Eur. J.* **2016**, *22*, 5261–5268.
[9] J. T. Hyde, K. Hanson, A. K. Vannucci, A. M. Lapides, L. Alibabaei, M. R. Norris, T. J. Meyer, D. P. Harrison, *ACS Appl. Mater. Interfaces* **2015**, *7*, 9554–9562.
[10] B. L. Wadsworth, A. M. Beiler, D. Khusnutdinova, S. I. Jacob, G. F. Moore, *ACS Catal.* **2016**, *6*, 8048–8057.
[11] Z. Chen, J. J. Concepcion, J. W. Jurss, T. J. Meyer, *J. Am. Chem. Soc.* **2009**, *131*, 15580–15581.
[12] D. L. Ashford, M. K. Gish, A. K. Vannucci, M. K. Brennaman, J. L. Templeton, J. M. Papanikolas, T. J. Meyer, *Chem. Rev.* **2015**, *115*, 13006–13049.
[13] L. Wu, M. Eberhart, A. Nayak, M. K. Brennaman, B. Shan, T. J. Meyer, *J. Am. Chem. Soc.* **2018**, *140*, 15062–15069.
[14] C. J. Kaminsky, J. Wright, Y. Surendranath, *ACS Catal.* **2019**, *9*, 3667–3671.
[15] M. N. Jackson, S. Oh, C. J. Kaminsky, S. B. Chu, G. Zhang, J. T. Miller, Y. Surendranath, *J. Am. Chem. Soc.* **2018**, *140*, 1004–1010.
[16] S. Oh, J. R. Gallagher, J. T. Miller, Y. Surendranath, *J. Am. Chem. Soc.* **2016**, *138*, 1820–1823.
[17] J. D. Blakemore, A. Gupta, J. J. Warren, B. S. Brunschwig, H. B. Gray, *J. Am. Chem. Soc.* **2013**, *135*, 18288–18291.
[18] X. Sala, S. Maji, R. Bofill, J. García-Antón, L. Escriche, A. Llobet, *Acc. Chem. Res.* **2014**, *47*, 504–516.
[19] M. D. Kärkäs, O. Verho, E. V. Johnston, B. Åkermark, *Chem. Rev.* **2014**, *114*, 11863–12001.
[20] X. Li, H. Lei, J. Liu, X. Zhao, S. Ding, Z. Zhang, X. Tao, W. Zhang, W. Wang, X. Zheng, R. Cao, *Angew. Chem. Int. Ed.* **2018**, *57*, 15070–15075.
[21] L. Xie, X. Li, B. Wang, J. Meng, H. Lei, W. Zhang, R. Cao, *Angew. Chem. Int. Ed.* **2019**, *58*, 18883–18887.
[22] P. Garrido-Barros, C. Gimbert-Suriñach, D. Moonshiram, A. Picón, P. Monge, V. S. Batista, A. Llobet, *J. Am. Chem. Soc.* **2017**, *139*, 12907–12910.
[23] L. Duan, F. Bozoglian, S. Mandal, B. Stewart, T. Privalov, A. Llobet, L. Sun, *Nat. Chem.* **2012**, *4*, 418–423.
[24] B. Zhang, L. Sun, *J. Am. Chem. Soc.* **2019**, *141*, 5565–5580.
[25] M. A. Hoque, M. Gil-Sepulcre, A. de Aguirre, J. A. A. W. Elemans, D. Moonshiram, R. Matheu, Y. Shi, J. Benet-Buchholz, X. Sala, M. Malfois, E. Solano, J. Lim, A. Garzón-Manjón, C. Scheu, M. Lanza, F. Maseras, C. Gimbert-Suriñach, A. Llobet, *Nat. Chem.* **2020**, *12*, 1060–1066.
[26] M. Nishio, *CrystEngComm* **2004**, *6*, 130.
[27] M. Nishio, *Tetrahedron* **2005**, *61*, 6923–6950.
[28] M. Ozawa, T. Ozawa, M. Nishio, K. Ueda, *J. Mol. Graphics Modell.* **2017**, *75*, 117–124.
[29] R. Matheu, L. Francàs, P. Chernev, M. Z. Ertem, V. Batista, M. Haumann, X. Sala, A. Llobet, *ACS Catal.* **2015**, *5*, 3422–3429.
[30] M. Gil-Sepulcre, J. O. Lindner, D. Schindler, L. Velasco, D. Moonshiram, O. Rüdiger, S. Debeer, V. Stepanenko, E. Solano, F. Würthner, A. Llobet, *J. Am. Chem. Soc.* **2021**, *143*, 11651–11661.
[31] R. N. Dürr, S. Chasvised, M. Gil-Sepulcre, A. Howe, M. A. Hoque, V. N'Guyen, S. Sadeghi, S. Reynaud, C. Cugnet, L. Authier, C. Gimbert-Suriñach, A. Bousquet, A. Llobet, L. Billon, *ACS Appl. Energ. Mater.* **2021**, *4*, 10534–10541.
[32] L. Wu, A. Nayak, J. Shao, T. J. Meyer, *Proc. Natl. Acad. Sci. USA* **2019**, *116*, 11153–11158.
[33] F. Li, K. Fan, L. Wang, Q. Daniel, L. Duan, L. Sun, *ACS Catal.* **2015**, *5*, 3786–3790.
[34] L. Wang, K. Fan, Q. Daniel, L. Duan, F. Li, B. Philippe, H. Rensmo, H. Chen, J. Sun, L. Sun, *Chem. Commun.* **2015**, *51*, 7883–7886.
[35] M. Schilling, R. A. Cunha, S. Luber, *J. Chem. Theory Comput.* **2020**, *16*, 2436–2449.
[36] N. Govindarajan, A. Tiwari, B. Ensing, E. J. Meijer, *Inorg. Chem.* **2018**, *57*, 13063–13066.
[37] J. L. Vallés-Pardo, M. C. Guijt, M. Iannuzzi, K. S. Joya, H. J. M. De Groot, F. Buda, *ChemPhysChem* **2012**, *13*, 140–146.
[38] J. M. de Ruiter, H. J. M. de Groot, F. Buda, *ChemCatChem* **2018**, *10*, 4594–4601.
[39] S. Zhan, R. Zou, M. S. G. Ahlquist, *ACS Catal.* **2018**, *8*, 8642–8648.
[40] J. Xia, F. Chen, J. Li, N. Tao, *Nat. Nanotechnol.* **2009**, *4*, 505–509.
[41] H. Cao, Z. Zhang, J.-W. Chen, Y.-G. Wang, *ACS Catal.* **2022**, *12*, 6606–6617.
[42] J. Poon, C. Batchelor-McAuley, K. Tschulik, R. G. Compton, *Chem. Sci.* **2015**, *6*, 2869–2876.
[43] X.-Y. Li, X.-F. Jin, X.-H. Yang, X. Wang, J.-B. Le, J. Cheng, *J. Chem. Phys.* **2023**, *158*, 084701.
[44] Y. Shao, J. M. De Ruiter, H. J. M. De Groot, F. Buda, *J. Phys. Chem. C* **2019**, *123*, 21403–21414.
[45] R. Car, M. Parrinello, *Phys. Rev. Lett.* **1985**, *55*, 2471–2474.
[46] T. D. Kühne, M. Iannuzzi, M. Del Ben, V. V. Rybkin, P. Seewald, F. Stein, T. Laino, R. Z. Khaliullin, O. Schütt, F. Schiffmann, D. Golze, J. Wilhelm, S. Chulkov, M. H. Bani-Hashemian, V. Weber, U. Borštnik, M. Taillefumier, A. S. Jakobovits, A. Lazzaro, H. Pabst, T. Müller, R. Schade, M. Guidon, S. Andermatt, N. Holmberg, G. K. Schenter, A. Hehn, A. Bussy, F. Belleflamme, G. Tabacchi, A. Glöß, M. Lass, I. Bethune, C. J. Mundy, C. Plessl, M. Watkins, J. VandeVondele, M. Krack, J. Hutter, *J. Chem. Phys.* **2020**, *152*, 194103.
[47] A. Laio, M. Parrinello, *Proc. Natl. Acad. Sci. USA* **2002**, *99*, 12562–12566.
[48] G. Bussi, A. Laio, *Nat. Rev. Phys.* **2020**, *2*, 200–212.
[49] J. Hénin, T. Lelièvre, M. R. Shirts, O. Valsson, L. Delemotte, *Living J. Comp. Mol. Sci.* **2022**, *4*, 1583.
[50] K. Chan, J. K. Nørskov, *J. Phys. Chem. Lett.* **2015**, *6*, 2663–2668.

[51] K. Chan, J. K. Nørskov, *J. Phys. Chem. Lett.* **2016**, *7*, 1686–1690.
[52] J. P. Menzel, H. J. M. De Groot, F. Buda, *J. Phys. Chem. Lett.* **2019**, *10*, 6504–6511.
[53] Y. Shao, H. J. M. De Groot, F. Buda, *ChemSusChem* **2021**, *14*, 479–486.
[54] S. Hammes-Schiffer, A. V. Soudackov, *J. Phys. Chem. B* **2008**, *112*, 14108–14123.
[55] A. D. Becke, *J. Chem. Phys.* **1993**, *98*, 5648–5652.
[56] C. Lee, W. Yang, R. G. Parr, *Phys. Rev. B* **1988**, *37*, 785–789.
[57] S. H. Vosko, L. Wilk, M. Nusair, *Can. J. Phys.* **1980**, *58*, 1200–1211.
[58] P. J. Stephens, F. J. Devlin, C. F. Chabalowski, M. J. Frisch, *J. Phys. Chem.* **1994**, *98*, 11623–11627.
[59] S. Grimme, J. Antony, S. Ehrlich, H. Krieg, *J. Chem. Phys.* **2010**, *132*, 154104.
[60] S. Grimme, S. Ehrlich, L. Goerigk, *J. Comput. Chem.* **2011**, *32*, 1456–1465.
[61] J. VandeVondele, J. Hutter, *J. Chem. Phys.* **2007**, *127*, 114105.
[62] M. Guidon, J. Hutter, J. VandeVondele, *J. Chem. Theory Comput.* **2009**, *5*, 3010–3021.
[63] G. Lippert, J. Hutter, M. Parrinello, *Mol. Phys.* **1997**, *92*, 477–487.
[64] S. Goedecker, M. Teter, J. Hutter, *Phys. Rev. B* **1996**, *54*, 1703–1710.
[65] M. Krack, *Theor. Chem. Acc.* **2005**, *114*, 145–152.
[66] J. P. Menzel, M. Kloppenburg, J. Belić, H. J. M. de Groot, L. Visscher, F. Buda, *J. Comput. Chem.* **2021**, *42*, 1885–1894.
[67] L. Duan, C. M. Araujo, M. S. G. Ahlquist, L. Sun, *Proc. Natl. Acad. Sci. USA* **2012**, *109*, 15584–15588.
[68] R. S. Mulliken, *J. Chem. Phys.* **1955**, *23*, 1833–1840.
[69] M. Bonomi, D. Branduardi, G. Bussi, C. Camilloni, D. Provasi, P. Raiteri, D. Donadio, F. Marinelli, F. Pietrucci, R. A. Broglia, M. Parrinello, *Comput. Phys. Commun.* **2009**, *180*, 1961–1972.
[70] W. Humphrey, A. Dalke, K. Schulten, *J. Mol. Graphics* **1996**, *14*, 33–38.

Manuscript received: January 29, 2024
Revised manuscript received: April 15, 2024
Accepted manuscript online: April 16, 2024
Version of record online: ■■, ■■

RESEARCH ARTICLE

A DFT-based MD simulation of a proton-coupled electron transfer (PCET) step in a Ru(bda)-based water oxidation oligomer catalyst anchored on a graphitic surface reveals dynamical stability of the system and vibrational resonances between CH-π stacking and charge fluctuations, fostering the PCET event.

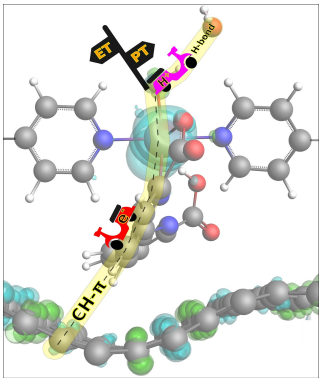

D. Calvani, R. Louwersheimer, Dr. F. Buda**